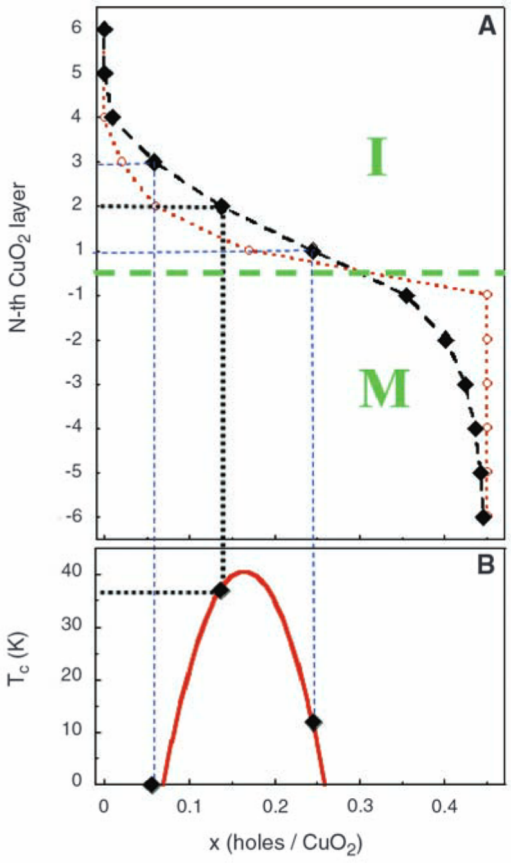

Fig. 4. Profile of charge carrier density across the LSCO-LCO interface. (**A**) The open dots represent the measured Sr concentration profile due to diffusion of Sr atoms from the LSCO layer to the LCO layer. Solid black dots show the charge carrier density in individual CuO_2 layers, as determined in this work. The nominal LSCO-LCO interface is between the layers $N = -1$ and $N = 1$. (**B**) The so-called generic phase diagram of HTS, i.e., the dependence of T_c on the carrier density. The dashed lines between (A) and (B) show interrelation between the charge profile across the interface and the corresponding T_c in the respective CuO_2 planes. Apparently, only the $N = 2$ CuO_2 plane is expected to have the value of T_c near that in optimally doped LSCO, whereas the overdoped $N = 1$ plane can have T_c as low as 10 K and the $N = 3$ plane is underdoped and may not be superconducting at all.

transistors) with ultrathin HTS electrodes transparent to electric and magnetic fields.

Apart from superconductivity (*15*, *26*), strongly correlated oxide heterostructures show a range of other fascinating interface electronic phenomena, including formation of high-mobility 2D electron gases, the quantum Hall effect, and magnetism (*27*–*29*). With the proper choice of dopant atoms to which the property of interest is most sensitive, our δ-doping tomography technique can also be applied to profile with atomic resolution these electronic states and to engineer the interface properties.

References and Notes

1. N. D. Mermin, H. Wagner, *Phys. Rev. Lett.* **17**, 1133 (1966).
2. V. L. Ginzburg, *Phys. Scr.* **T27**, 76 (1989).
3. V. L. Berezinskii, *Sov. Phys. JETP* **32**, 493 (1971).
4. J. M. Kosterlitz, D. J. Thouless, *J. Phys. Chem.* **6**, 1181 (1973).
5. E. Dagotto, *Rev. Mod. Phys.* **66**, 763 (1994).
6. P. A. Lee, N. Nagaosa, X. G. Wen, *Rev. Mod. Phys.* **78**, 17 (2006).
7. I. Bozovic, J. N. Eckstein, in *Physical Properties of Superconductors, Vol. 5*, D. M. Ginsberg, Ed. (World Scientific, Singapore, 1996), pp. 99–207.
8. J. M. Triscone, Ø. Fischer, *Rep. Prog. Phys.* **60**, 1673 (1997).
9. T. Sugimoto *et al.*, *Appl. Phys. Lett.* **58**, 1103 (1991).
10. T. Terashima *et al.*, *Phys. Rev. Lett.* **67**, 1362 (1991).
11. I. Bozovic, J. N. Eckstein, G. F. Virshup, *Physica C* **235–240**, 178 (1994).
12. M. Calame *et al.*, *Phys. Rev. Lett.* **86**, 3630 (2001).
13. A. Rüfenacht *et al.*, *Solid State Electron.* **47**, 2167 (2003).
14. I. Hetel, T. R. Lemberger, M. Randeria, *Nat. Phys.* **3**, 700 (2007).
15. A. Gozar *et al.*, *Nature* **455**, 782 (2008).
16. H. Zhou *et al.*, http://arxiv.org/abs/0903.2097 (2009).
17. S. Smadici *et al.*, *Phys. Rev. Lett.* **102**, 107004 (2009).
18. M. Basletic *et al.*, *Nat. Mater.* **7**, 621 (2008).
19. A. Ohtomo, D. A. Muller, J. L. Grazul, H. Y. Hwang, *Nature* **419**, 378 (2002).
20. I. Bozovic, *IEEE Trans. Appl. Supercond.* **11**, 2686 (2001).
21. See supporting material on *Science* Online.
22. J. W. Loram, K. A. Mirza, P. F. Freeman, *Physica C* **171**, 243 (1990).
23. H. Alloul *et al.*, *Phys. Rev. Lett.* **67**, 3140 (1991).
24. C. Bernhard *et al.*, *Phys. Rev. Lett.* **77**, 2304 (1996).
25. K. Karpinska *et al.*, *Phys. Rev. Lett.* **84**, 155 (2000).
26. N. Reyren *et al.*, *Science* **317**, 1196 (2007); published online 1 August 2007 (10.1126/science.1146006).
27. A. Ohtomo, H. Y. Hwang, *Nature* **427**, 423 (2004).
28. A. Tsukazaki *et al.*, *Science* **315**, 1388 (2007); published online 24 January 2007 (10.1126/science.1137430).
29. A. Brinkman *et al.*, *Nat. Mater.* **6**, 493 (2007).

30. We thank V. L. Ginzburg, D. Schlom, B. Halperin, and S. Kivelson for useful discussions. Supported by the U.S. Department of Energy under contract MA-509-MACA.

Supporting Online Material

www.sciencemag.org/cgi/content/full/326/5953/699/DC1
Materials and Methods
Figs. S1 to S7
References

9 July 2009; accepted 24 August 2009
10.1126/science.1178863

Reconstruction of Molecular Orbital Densities from Photoemission Data

Peter Puschnig,[1]* Stephen Berkebile,[2] Alexander J. Fleming,[2] Georg Koller,[2] Konstantin Emtsev,[3] Thomas Seyller,[3] John D. Riley,[4] Claudia Ambrosch-Draxl,[1] Falko P. Netzer,[2] Michael G. Ramsey[2]

Photoemission spectroscopy is commonly applied to study the band structure of solids by measuring the kinetic energy versus angular distribution of the photoemitted electrons. Here, we apply this experimental technique to characterize discrete orbitals of large π-conjugated molecules. By measuring the photoemission intensity from a constant initial-state energy over a hemispherical region, we generate reciprocal space maps of the emitting orbital density. We demonstrate that the real-space electron distribution of molecular orbitals in both a crystalline pentacene film and a chemisorbed *p*-sexiphenyl monolayer can be obtained from a simple Fourier transform of the measurement data. The results are in good agreement with density functional calculations.

Highest occupied and lowest unoccupied electronic orbitals of molecules are the prime determinants of the respective compounds' chemical, electronic, and optical properties. The electronic states of extended periodic systems are described by band structures, allowed energies E for given momentum values k, and the orbitals are Bloch wave functions associated with a particular k point. For finite systems, such as molecules, the orbitals are viewed as a particular spatial distribution of the electron density at discrete energies. Several experimental methods have enabled imaging of molecular orbitals under certain conditions (*1*). For simple diatomic molecules in the gas phase, high harmonic generation using femtosecond laser pulses allows a tomographic reconstruction of the highest occupied molecular orbital (HOMO) (*2*). Electron momentum spectroscopy, also applied to molecules in the gas phase, can provide the spherically averaged orbital electron density in momentum space (*3*). In the solid state, scanning tunneling microscopy (STM) is a powerful technique for mapping orbital structures of more complex molecules, particularly at cryogenic temperatures on inert decoupling layers (*4*). However, strong bonding interactions with the substrate complicate interpretation of the

[1]Chair of Atomistic Modelling and Design of Materials, University of Leoben, 8700 Leoben, Austria. [2]Institute of Physics, Karl-Franzens University Graz, 8010 Graz, Austria. [3]Lehrstuhl für Technische Physik, Universität Erlangen-Nürnberg, 91058 Erlangen, Germany. [4]Department of Physics, La Trobe University, Victoria 3086, Australia.

*To whom correspondence should be addressed. E-mail: peter.puschnig@unileoben.ac.at

images (*5*), making complementary experimental techniques desirable. Here we demonstrate that ultraviolet angle-resolved photoelectron spectroscopy (ARPES) allows molecular orbital densities to be reconstructed in real space in a rather simple way, as exemplified by analyses of a crystalline pentacene film and a chemisorbed monolayer, *p*-sexiphenyl on Cu (110).

In ARPES (schematically depicted in Fig. 1), an incident photon of energy $\hbar\omega$ excites an electron from a bound initial state, described by wave function ψ_i and energy E_i, to a final electron state ψ_f with kinetic energy E_{kin}. Because energy and momentum parallel to the surface are conserved during the photoemission process, the measurement of the emitted electron's energy and momentum probes the band structure of solids. ARPES is commonly used to study band dispersions, Fermi surfaces, and many-body correlations in a wide range of materials (*6*). A theoretical description of the angle-resolved photocurrent intensity is generally rather involved, and attempts to analyze it in a quantitative manner are rather scarce.

In this work, we treat the photo-excitation as a single coherent process from a molecular orbital to the final state, which is referred to as the one-step model of photoemission (PE). The PE intensity $I(\theta,\phi;E_{kin})$ is given by a Fermi golden rule formula (*7*).

$$I(\theta,\phi;E_{kin}) \propto \sum_i |\langle\psi_f(\theta,\phi;E_{kin})|\mathbf{A}\cdot\mathbf{p}|\psi_i\rangle|^2 \times \delta(E_i + \Phi + E_{kin} - \hbar\omega) \quad (1)$$

Here, the polar and azimuthal emission angles defined in Fig. 1 are denoted by θ and ϕ, respectively. The photocurrent I is given by a sum over all transitions from occupied initial states i described by wave functions ψ_i to the final state ψ_f characterized by the direction (θ,ϕ) and the kinetic energy of the emitted electron. The δ function ensures energy conservation, where Φ denotes the sample work function. The transition matrix element is given in the dipole approximation, where $\mathbf{p}$ and $\mathbf{A}$, respectively, denote the momentum operator and the vector potential of the exciting electro-magnetic wave. The difficulty in evaluating Eq. 1 lies in the proper treatment of the final state. In the most simple approach, it is approximated by a plane wave (PW) characterized only by the direction and wave number of the emitted electron. This has already been proposed more than 30 years ago (*8*), with some success in explaining the observed PE distribution from atoms and small molecules adsorbed at surfaces. Using a PW approximation is appealing because the evaluation of Eq. 1 renders the photocurrent I_i arising from one particular initial state i proportional to the Fourier transform (FT) $\tilde{\psi}_i(\mathbf{k})$ of the initial-state wave function corrected by the polarization factor $\mathbf{A}\cdot\mathbf{k}$:

$$|\tilde{\psi}_i(\mathbf{k})| \propto \frac{\sqrt{I_i(\theta,\phi)}}{|\mathbf{A}\cdot\mathbf{k}|} \quad (2)$$

Thus, if the angle-dependent photocurrent of individual initial states can be selectively measured (as it can for organic molecules where the intermolecular band dispersion is often smaller than the energetic separation of individual orbitals), a one-to-one relation between the photocurrent and the molecular orbitals in reciprocal space can be established. This allows the measurement of the absolute value of the initial-state wave function in reciprocal space and, via a subsequent FT, a reconstruction of molecular orbital densities in real space.

However, attempts to explain ARPES data of oriented films of large polyatomic molecules by a PW final state led to the conclusion that it should not be used in this context (*9*, *10*) because it does not take into account spherical wave effects of the outgoing wave. Thus, the independent atomic center (IAC) approximation was adopted by calculating the emission as an independent, but coherent, sum from individual atomic centers (*11*). The IAC approximation has been used to account for the observed take-off angle dependence of the photocurrent of thin films of organic molecules (*12*). As a further improvement over the IAC, single-scattering (SS) events of the emitted electron have also been taken into account and shown to be important in some applications (*13*, *14*). Here we argue that, despite the obvious simplification of the PW final-state assumption over the more accurate IAC and SS theories, the PW assumption can still lead to a meaningful description of the observed PE intensity of large π-conjugated molecules. As already noted by Grobman (*11*), the IAC expression for the photocurrent can be considerably simplified if the initial molecular orbital comprises atomic orbitals of the same chemical and orbital character. This situation is met by a π molecular orbital of a planar polyatomic molecule for which the contributing atomic orbitals are all of p_z character. For such a case, we show in the supporting online material (SOM) that the angular-dependent photocurrent, computed within the IAC approximation, is given by the FT of the initial state modulated only by a weakly angular-dependent function (*15*). Furthermore, for the special case where the electric field vector of the photon is parallel to the direction of the emitted electron, the IAC reduces exactly to Eq. 2 (*15*, *16*). Thus, the PW final-state assumption can be expected to be valid if the following conditions are fulfilled: (i) π-orbital emissions from large planar molecules; (ii) an experimental geometry in which the angle between the polarization vector $\mathbf{A}$ and the direction of the emitted electron $\mathbf{k}$ is rather small

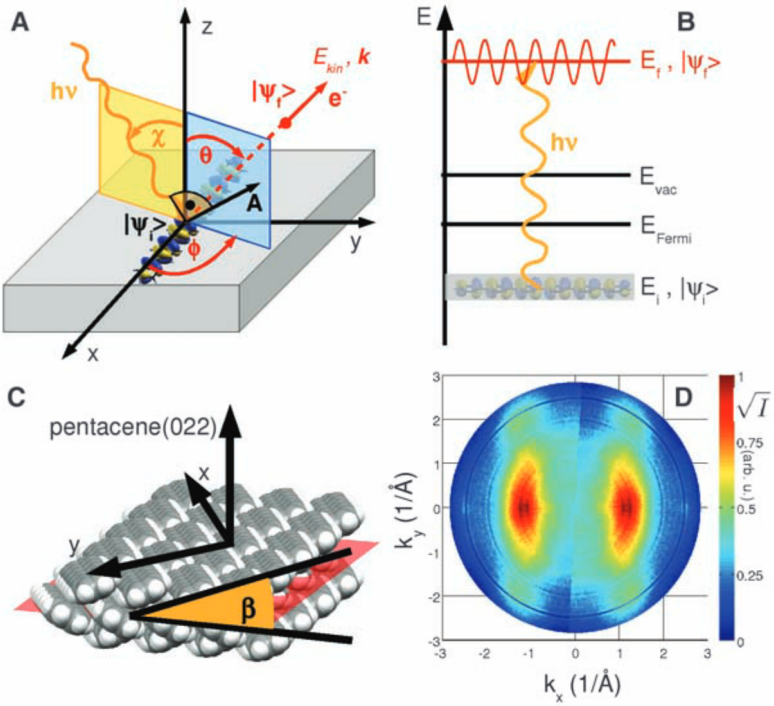

Fig. 1. Momentum maps in angle-resolved PE experiments. (**A**) The incident photon with energy $h\nu$ and vector potential **A** excites an electron from the initial state ψ_i to the final state ψ_f characterized by the kinetic energy E_{kin} and the momentum vector **k**. The polar and azimuthal angles θ and ϕ, respectively, define the direction of the photoemitted electron. (**B**) Schematic energy-level diagram showing the energy of the initial state E_i, the Fermi level E_{Fermi}, the vacuum level E_{vac}, and the final-state energy E_f. (**C**) Model of the pentacene multilayer arrangement on a Cu(110)-(2 × 1)O surface: The long molecular axis points along the *x* axis, and the (022) surface (indicated by the red plane) features pentacene molecules tilted by $\beta = 26°$ out of the *xy* plane. (**D**) Square root of the PE intensity as a function of azimuthal and polar angle after conversion to momentum (azimuthal scan) at a constant binding energy of 1.3 eV ($h\nu$ = 35 eV) corresponding to the pentacene HOMO.

(Fig. 1A); and (iii) molecules consisting of many light atoms (H, C, N, O). The third requirement is a result of the small scattering cross section of light atoms and the presence of many scattering centers expected to lead to a rather weak and structureless angular pattern (*14*, *17*). In the SOM, we compare the PW approach with calculations within the framework of the IAC and SS theories from the literature for a typical π-conjugated organic molecule satisfying the above-mentioned conditions, thereby demonstrating the agreement among the theoretical results as well as with the experimental data (*15*).

We continue by demonstrating the viability of the PW approach for both reciprocal space mapping as well as real-space reconstructions of relatively complicated molecular orbitals. We first present results for the organic π-conjugated molecular semiconductor pentacene in a multilayer thin film, focusing on the emission from the HOMO. As a second example, we show that the approach allows reconstruction of the orbitals of *p*-sexiphenyl bonded to the Cu (110) surface. Not only do we reconstruct a real-space image of the HOMO, but we also show that the PE intensity at the Fermi level that appears on adsorption has the orbital structure of the lowest unoccupied molecular orbital (LUMO).

Pentacene is a planar aromatic molecule consisting of five linearly edge-fused phenyl rings, and has been extensively studied owing to its interesting optoelectronic properties. Its electronic structure, in particular the intermolecular HOMO dispersion, has been analyzed by means of both PE experiments (*18*–*20*) and calculations within the framework of density functional theory (DFT) (*21*–*23*). When the molecule is vacuum deposited on the p(2 × 1) oxygen-reconstructed Cu(110) surface, its long axis orients parallel to the oxygen rows, resulting in crystalline pentacene(022) films (*24*) (Fig. 1C). The (022) surface termination exhibits molecules with their long axis parallel to the surface but with the π face tilted out of the surface plane by an angle of β = 26°. Figure 1D shows a momentum map at the HOMO energy of a pentacene multilayer using a toroidal electron energy analyzer at the synchrotron radiation facility BESSY II (*25*). As a function of the momentum vector parallel to the molecular axis, k_x, there is a pronounced intensity maximum of the PE intensity centered at 1.15 $Å^{-1}$, as observed previously (*20*). In the momentum maps, these intense features extend about ±0.8 $Å^{-1}$ in the k_y direction, and in addition, there are weaker-intensity lobes at about the same k_x value around $k_y \approx \pm 2$ $Å^{-1}$.

To illustrate the relation between the measured PE intensity and the FT of the emitting orbital, we calculate the electronic structure of an isolated pentacene molecule using DFT (*26*). The resulting HOMO orbital is depicted in Fig. 2A, and its corresponding three-dimensional FT in Fig. 2B. Because the momentum maps are measured at constant binding energy, we evaluate the FT on a hemisphere of radius $k = \sqrt{(2m/\hbar^2)E_{kin}}$ (indicated in red). The value of the FT on that hemisphere for a kinetic energy of 29.8 eV is shown in Fig. 2C. However, a comparison with the photoelectron momentum map (Fig. 1D) appears to be unsatisfactory. In particular, the minimum at $k_y = 0$, reflecting the nodal structure of the pentacene HOMO, seems to be absent in the measurement. The reason for this apparent discrepancy is a geometric one: the presence of both +26° and −26° tilt angles β in the film structure. Once this factor is taken into account, the agreement between experiment (Fig. 1D) and theory (Fig. 2D) is excellent. Both the strong maxima at $k_y = 0$ and the weak peaks at $k_y = 2$ $Å^{-1}$ result from the out-of-plane tilt angle of the pentacene molecules (*15*). Clearly, the FT approach describes the PE intensity well and therefore allows molecular orientations to be determined with a precision comparable to that of standard in situ techniques such as near-edge x-ray absorption fine structure (NEXAFS). By varying the tilt angle β in the simulations, we estimate the accuracy of the ARPES approach to be better than 5° (fig. S3). A comparison between the PE intensity and the FT has the added advantage that rather than giving an average orientation, multiple orientations are immediately apparent and can be resolved. Moreover, ARPES works at low photon energies, minimizing damage to the sample, and does not require a tunable photon source.

We next apply the approach to an adsorbed monolayer bound to a metal surface. *p*-Sexiphenyl adsorbs on the Cu(110) surface with its molecular planes parallel to the surface, and orients with its long axis parallel to the Cu rows (*27*), as seen in the STM image in fig. S2B. Upon the adsorption of the molecules, we recognize two new features in the low–binding energy region in the ARPES data acquired parallel to the molecular axis (fig. S2C): one centered at 0.3 eV below the Fermi level, and the other at a binding energy of 1.9 eV at the intersection of the Cu sp and d bands. Momentum maps at these two binding energies (Fig. 3, A and C, respectively) compare well to the calculated FTs of the HOMO and LUMO from an isolated sexiphenyl (Fig. 3, B and D). The main characteristics, maxima at $k_x^{HOMO} \approx \pm 1.45$ $Å^{-1}$ reflecting the spatial periodicity set by the length of one phenyl ring ($2\pi/k_x^{HOMO} \approx 4.3$ Å) (*28*), are observed in the data as well as in the calculation. Also, the width Δk_x, which is inversely proportional to the length of the molecule, appears consistent in the PE data. The same holds for the extension in *y* direction, Δk_y, which is related to the width of a phenyl ring. These findings are

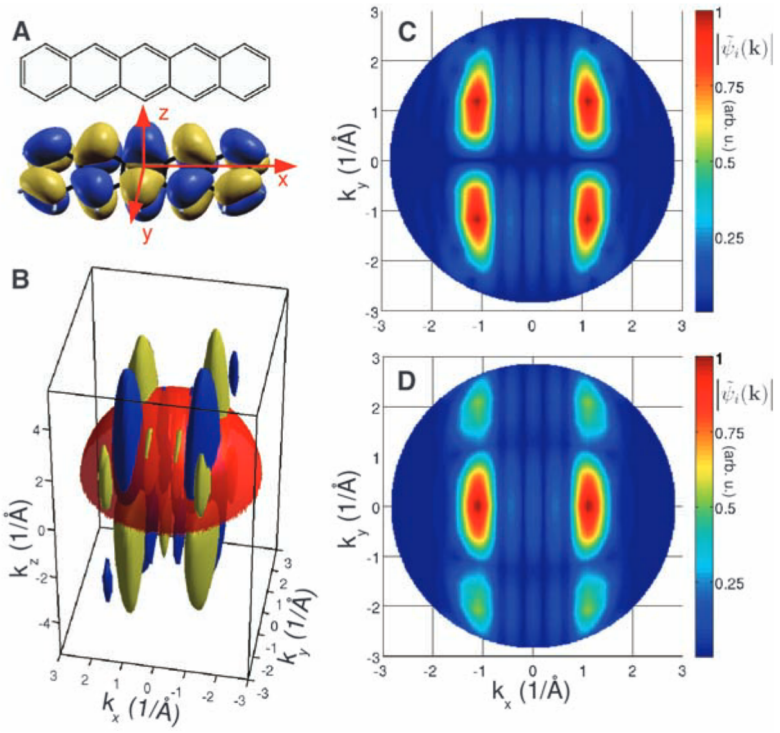

Fig. 2. Calculation of the PE intensity from the FT of the molecular orbital. (**A**) Line drawing and HOMO of pentacene as obtained from a DFT calculation for an isolated molecule. The choice of the coordinate system is indicated, where *x* and *y* are parallel to the long and short molecular axis, respectively, and *z* is perpendicular to the molecular plane. (**B**) Three-dimensional FT of the HOMO as an isosurface plot; blue indicates negative and yellow, positive values, together with a hemisphere of radius $k = \sqrt{(2m/\hbar^2)E_{kin}}$ with a kinetic energy $E_{kin} = 29.8$ eV (see text). (**C**) Absolute value of the HOMO FT on the hemisphere shown in (B). (**D**) Simulation of PE intensity of the pentacene multilayer film, taking into account molecules with tilt angles of β = +26° and β = −26° out of the *xy* plane (see text).

strong evidence that the molecular feature observed at a binding energy of 1.9 eV can indeed be attributed to the sexiphenyl HOMO and, moreover, that its character is preserved even in a strongly interacting monolayer on a metal surface. In a similar manner, we unambiguously assign the intensity close to the Fermi level to an emission from the filled LUMO (Fig. 3, C and D). This emission thus indicates electron transfer from the metal into the former LUMO of the isolated molecule; as was the case for the HOMO, the nodal structure of the LUMO is found to be preserved on adsorption. Thus, PE momentum maps provide fingerprints of molecular states, allowing for their unique identification even in cases where there is a rather strong bonding interaction.

The ability to reproduce the PE momentum maps with FTs of the initial-state wave functions encouraged us to reconstruct real-space images of the molecular orbital densities from the experimental PE data. From Eq. 2, we take the square root of the PE data and divide it by the polarization factor $|\mathbf{A}\cdot\mathbf{k}| \propto |\sin\theta\cos\chi - \cos\theta\sin\chi|$. Restricting the data to positive k_x values and considering the incidence angle $\chi = -40°$ of the p-polarized photons (Fig. 1A), this function has a maximum for a take-off angle $\theta = 50°$ and a minimum value of 0.64 at normal emission. Before performing the inverse FT of the processed PE data, we mirror the data to the negative k_x plane and change its sign (or leave it unchanged) according to the parity of the wave function, which is even for the HOMO (and odd for the LUMO). By the latter procedure, we restore phase information on the wave function to facilitate the comparison with calculated orbitals. The inverse FTs of the PE data for the adsorbed sexiphenyl HOMO and LUMO are compared with the DFT calculated orbitals of the isolated molecule in Fig. 4. Spatial periodicities and nodal structure are well conserved across theory and experiment. Because the resolution Δx in the reconstructed images is inversely proportional to the PW cutoff k_{max} (thus $\Delta x = \pi/k_{max}$), kinetic energies of around 30 eV as used in our experiments lead to $\Delta x \approx 1$ Å.

Compared to the DFT orbitals, both the HOMO and LUMO electron densities obtained from photoemission are more weighted around the center of the molecule, a distinction we tentatively attribute to the interaction with the Cu surface. Indeed, in sexiphenyl charge-transfer salts, the local distortions and the transferred electrons are located around the center of the molecule (*29*). Further-

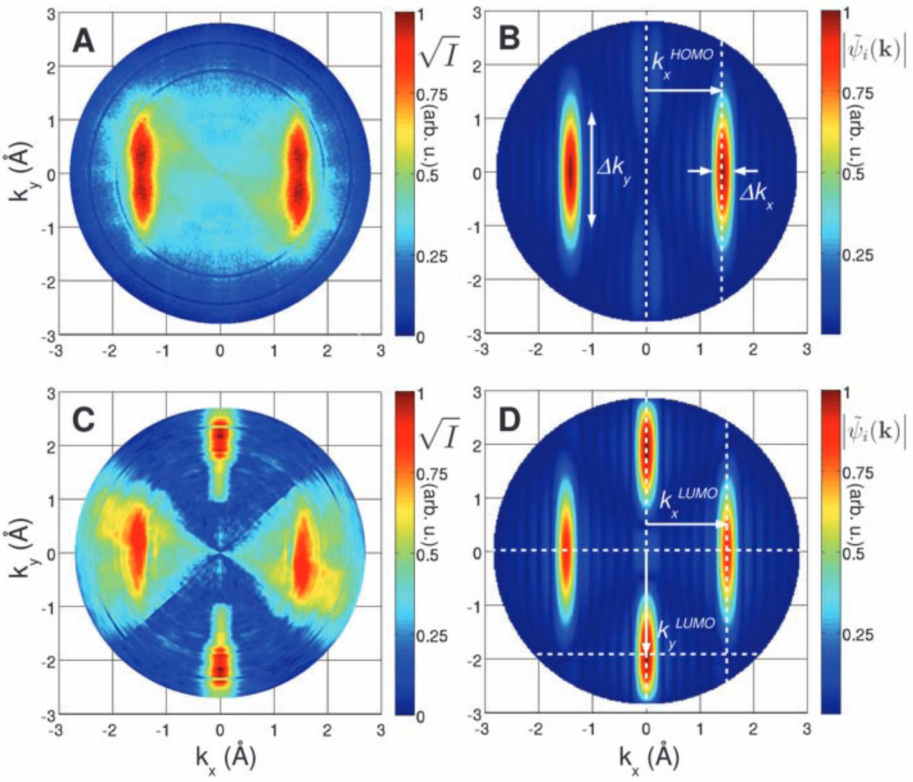

Fig. 3. Measured PE intensities compared to calculated FTs. (**A**) PE momentum map (square root of the intensity) from a monolayer of sexiphenyl on Cu(110) at a binding energy of 1.9 eV, which corresponds to the sexiphenyl HOMO. (**B**) Absolute value of the FT of the sexiphenyl HOMO calculated for an isolated molecule within DFT. (**C**) Same as in (A) but for a binding energy of 0.3 eV. (**D**) Same as in (B) but for the sexiphenyl LUMO. Characteristic features in the computed FTs are indicated by the white arrows, as described in the text.

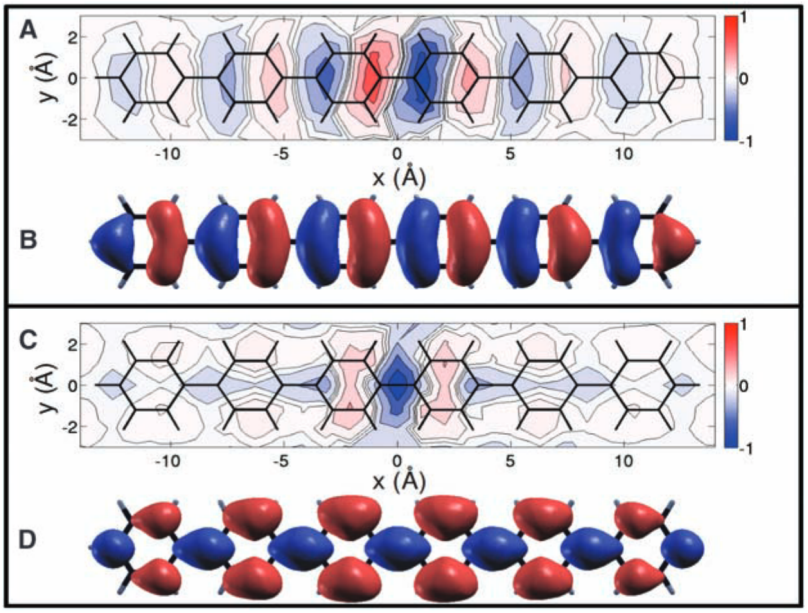

Fig. 4. Molecular orbitals reconstructed from PE data as compared to DFT orbitals. (**A**) The HOMO of sexiphenyl reconstructed from the PE momentum map at a binding energy of 1.9 eV. (**B**) HOMO of an isolated sexiphenyl molecule from DFT. (**C**) The LUMO of sexiphenyl reconstructed from the momentum map at a binding energy of 0.3 eV. (**D**) LUMO of an isolated sexiphenyl molecule from DFT. Experimentally determined orbitals are displayed as density plots, where red colors indicate positive and blue, negative values. For clarity, isolines (dashed lines) are also included. The DFT orbitals are represented as isosurface plots using the same color code. The molecular backbone is indicated by black lines.

more, although STM images typically do not match molecular orbital images exactly, an STM image of a monolayer of sexiphenyl adsorbed on Cu (110) does show an electron density distribution that is weighted toward the center of the molecules (fig. S2B). Nonetheless, improvements in the PE signal-to-background ratio are necessary before any strong conclusions can be reached concerning the extent of orbital distortion introduced by the metal surface.

The demonstrated simple relation between the PE intensity and the FT of the molecular orbital should be a valuable tool for further investigation of organic molecular films and monolayers.

References and Notes

1. W. H. E. Schwarz, *Angew. Chem. Int. Ed.* **45**, 1508 (2006).
2. J. Itatani *et al.*, *Nature* **432**, 867 (2004).
3. C. E. Brion, G. Cooper, Y. Zheng, I. V. Litvinyuk, I. E. McCarthy, *Chem. Phys.* **270**, 13 (2001).
4. J. Repp, G. Meyer, S. M. Stojkovic, A. Gourdon, C. Joachim, *Phys. Rev. Lett.* **94**, 026803 (2005).
5. R. Temirov, S. Soubatch, O. Neucheva, A. C. Lassise, F. S. Tautz, *N. J. Phys.* **10**, 053012 (2008).
6. A. Damascelli, *Phys. Scr.* **T109**, 61 (2004).
7. P. J. Feibelman, D. E. Eastman, *Phys. Rev. B* **10**, 4932 (1974).
8. J. W. Gadzuk, *Phys. Rev. B* **10**, 5030 (1974).
9. T. Permien, R. Engelhardt, C. A. Feldmann, E. E. Koch, *Chem. Phys. Lett.* **98**, 527 (1983).
10. N. V. Richardson, *Chem. Phys. Lett.* **102**, 390 (1983).
11. W. D. Grobman, *Phys. Rev. B* **17**, 4573 (1978).
12. S. Hasegawa *et al.*, *Phys. Rev. B* **48**, 2596 (1993).
13. N. Ueno *et al.*, *J. Chem. Phys.* **107**, 2079 (1997).
14. S. Kera *et al.*, *Chem. Phys.* **325**, 113 (2006).
15. Additional details of sample preparation, experimental setup, and computational methods are available as supporting online material on *Science* Online.
16. S. M. Goldberg, C. S. Fadley, S. Kono, *Solid State Commun.* **28**, 459 (1978).
17. E. L. Shirley, L. J. Terminello, A. Santoni, F. J. Himpsel, *Phys. Rev. B* **51**, 13614 (1995).
18. N. Koch *et al.*, *Phys. Rev. Lett.* **96**, 156803 (2006).
19. H. Kakuta *et al.*, *Phys. Rev. Lett.* **98**, 247601 (2007).
20. S. Berkebile *et al.*, *Phys. Rev. B* **77**, 115312 (2008).
21. M. L. Tiago, J. E. Northrup, S. G. Louie, *Phys. Rev. B* **67**, 115212 (2003).
22. K. Hummer, C. Ambrosch-Draxl, *Phys. Rev. B* **72**, 205205 (2005).
23. D. Nabok *et al.*, *Phys. Rev. B* **76**, 235322 (2007).
24. M. Koini *et al.*, *Thin Solid Films* **517**, 483 (2008).
25. L. Broekman *et al.*, *J. Electron. Spectrosc. Relat. Phenom.* **144–147**, 1001 (2005).
26. X. Gonze *et al.*, *Comput. Mater. Sci.* **25**, 478 (2002).
27. M. Oehzelt *et al.*, *ChemPhysChem* **8**, 1707 (2007).
28. G. Koller *et al.*, *Science* **317**, 351 (2007).
29. M. G. Ramsey, M. Schatzmayr, S. Stafström, F. P. Netzer, *Europhys. Lett.* **28**, 85 (1994).

30. This work was supported by the Austrian Science Foundation (FWF) within the National Research Network S97 "Interface Controlled and Functionalized Organic Films." The ARPES data for this work were measured at the beamline TGM4 of the Helmholtz Zentrum Berlin—Electron storage ring BESSY II supported by the European Community–Research Infrastructure Action under FP7 Programme for Research and Technical Development through the Integrated Infrastructure Initiative "European Light Sources Activities–Synchrotrons and Free Electron Lasers–Grant Agreement 226716."

Supporting Online Material

www.sciencemag.org/cgi/content/full/1176105/DC1
SOM Text
Figs. S1 to S5
References

11 May 2009; accepted 6 August 2009
Published online 10 September 2009;
10.1126/science.1176105
Include this information when citing this paper.

Synergic Sedation of Sensitive Anions: Alkali-Mediated Zincation of Cyclic Ethers and Ethene

Alan R. Kennedy,[1] Jan Klett,[1] Robert E. Mulvey,[1]* Dominic S. Wright[2]

Deprotonation of alkyl and vinyl carbon-hydrogen bonds for synthetic purposes is often hindered not merely by the need for an exceptionally strong base, but by the inherent instability of the resultant anion. Metalation of cyclic ethers adjacent to oxygen, for example, has invariably initiated a ring-opening decomposition pathway. Here, we show that the use of a bimetallic base can overcome such instability through a cooperative combination of zinc-carbon and sodium-oxygen bonding. Both tetrahydrofuran and tetrahydropyran reacted cleanly over days at room temperature to yield α-zinc–substituted products that were sufficiently stable to be isolated and crystallographically characterized. A related zincation-anion trapping strategy, with sodium replaced by potassium, induced clean deprotonation of ethene to yield a stable product. Preliminary electrophilic quenching experiments with the α-zinc–substituted cyclic ethers and benzoyl chloride gave satisfactory yields of the tetrahydrofuran-derived ketone but only trace amounts of the tetrahydropyran-derived ketone.

Transforming relatively inert carbon-hydrogen bonds to more reactive, more useful carbon-metal bonds, or metalation, is an essential tool for constructing compounds. Metalation is usually performed with organolithium reagents because the high electropositivity of lithium leads to polar, reactive $C^{\delta-}$- $Li^{\delta+}$ bonds, which can metalate C-H bonds in organic compounds. Despite their widespread use, organolithium reagents (*1*, *2*) have major limitations, including an inability to metalate low-acidity hydrocarbons (that is, those with high pK_a values, where K_a is the acid dissociation constant). A pertinent example would be ethene, the simplest alkene, which has very weakly acidic H atoms (its estimated pK_a is ~44) (*3*); and although ethene's carbometalation (RLi addition across the C=C bond) and polymerization are common, its metalation in contrast is exceedingly difficult and to date has only been achieved in a few select cases with aggressive, structurally ill-defined superbasic mixtures. Other common drawbacks with organolithium reagents are poor functional group tolerance and low stability of lithiohydrocarbon intermediates. Seeking improved metalating agents, a few groups worldwide have recently pioneered bimetallic alternatives. Notable examples include the lithium zincate $LiZn^tBu_2(TMP)$ [where TMP = 2,2,6,6-tetramethylpiperidide, *cyclo*-$NC(Me)_2(CH_2)_3C(Me)_2$] made by Kondo and Uchiyama and colleagues (*4*) and the lithium magnesiate (TMP)MgCl.LiCl made by Knochel and colleagues (*5*), both of which can selectively metalate a wide variety of aromatic compounds. Bimetallic bases can also effect unusual regioselectivities, as we have shown with the sodium magnesiate [(TMEDA)Na(TMP)(^{n}Bu)Mg(TMP)] (where TMEDA = N,N,N',N'-tetramethylethylenediamine, $Me_2NCH_2CH_2NMe_2$), which metalates toluene in the meta position (*6*), in contrast to the common lateral- and ortho-metalation of aromatic compounds that occurs with conventional bases.

Metalation of ethers is also particularly challenging because metalated ethers are generally highly unstable and rapidly cleave. Such metal-induced ether cleavage is extremely complicated, with several different pathways possible (*7*). With strong bases such as organolithium reagents, metalation (exchange of a C-H bond for a C-metal bond) is generally the opening attack leading to the breakdown of the ether ("protophilic ether cleavage") (*8*). Specifically with the cyclic tetrahydrofuran (THF), metalation at the α-position localizes a high degree of negative charge on the α-C atom adjacent to the electron-rich O atom, causing a severe destabilization that incites a spontaneous ring opening. The final decomposition products depend on conditions, but a mixture of ethene and the enolate of acetaldehyde is common (Fig. 1) (*9*).

Synthetically useful controlled metalation of THF would therefore appear to be an insurmountable challenge. However, we report successful metalation achieved by using a synergic mixed-metal strategy that has far-reaching implications for metalation and organometallic chemistry in general. By mixing an alkali metal with zinc in the same coordination compound, or "alkali-metal–mediated zincation" (AMM*Zn*) (*10*–*12*), we show that not only is it possible to directly metalate (zincate) the

[1]WestCHEM, Department of Pure and Applied Chemistry, University of Strathclyde, Glasgow G1 1XL, UK. [2]Chemistry Department, Cambridge University, Lensfield Road, Cambridge CB2 1EW, UK.

*To whom correspondence should be addressed. E-mail: r.e.mulvey@strath.ac.uk